Permeability controlling factors extracted from 3D images of carbonate rocks

Nathaly L. Archilha[1,2], Roseane M. Missagia[1], Cathy Hollis[2], Marco A. R. de Ceia[1], Samuel A. McDonald[3], Irineu A. Lima Neto[1], David S. Eastwood[3], Peter Lee[3]

[1] North Fluminense State University, Brazil (UENF/LENEP), [2] School of Earth, Atmospheric and Environmental Sciences - The University of Manchester, [3] School of Materials (The Manchester X-ray Imaging Facility) – The University of Manchester

Abstract

Pore geometrical parameters derived from digital image analysis (DIA) of thin sections have recently been used to improve the coefficient of determination (R^2) of permeability versus porosity (e.g. Weger et al., 2009). Despite an great improvement was observed, no spatial information of the pore structure was considered, as DIA parameters were obtained from 2D datset analysis. Here, we link pore space parameters, obtained from 3D images, to experimental physical properties of carbonate rocks to improve permeability predictions. Results show that applying a combination of porosity, pore size and 3D geometrical parameters to permeability significantly improves the adjusted coefficient of determination ($\overline{R}^2$). These results can be interpreted to reflect a pore geometrical and pore size control of permeability prediction.

Introduction

A large fraction of the world's hydrocarbons are stored in carbonates rocks, which are highly prone to post-depositional alteration, that modifies the pore structure, creating or destroying porosity, changing permeability and acoustic properties (Hollis et al., 2010; Castro and Rocha, 2013).

Carbonate rocks present a wide range of permeability for the same porosity value due to a marked variability in the connectivity of pores, both with respect to average coordination number and pore throat diameter (Ahr, 2008). Jivkov et al. (2013) demonstrated that coordination number is a more important control parameter on permeability than total porosity. However, pore geometry, pore throat radius and coordination number cannot be reliably quantified using thin sections images, as three-dimensional information cannot be assessed, X-ray tomography can be used to determine these parameters and also to visualize the pore and matrix structures. In this study, we show how information regarding pore space, obtained by X-ray tomography, can improve the prediction of permeability on a suite of Albian carbonate rocks. We extract tortuosity, coordination number, pore shape, size and volume, from 3D images of the pore space and incorporate them into Kozeny model for permeability estimation.

Reservoir Geology

In this study, a suite of Post-Salt, Albian carbonates from two neighboring wells (W1 and W2) within the Campos Basin (Figure 1) were analysed The suite is mostly composed of grainstones and packstones containing oncolites, peloids, oolites and bioclasts. Here, the focus was on ooliticgrainstones (og) and cemented grainstones (cg). Oncolite/oolite-rich skeletal grainstones and clean packstones comprise the best quality reservoir facies with porosity ranging from 20 to 34% and permeability reaching values of 2000 mD, and usually greater than 100 mD (Bruhn et al., 2003). The samples comprise more than 95% calcium carbonate with minor (< 2%) detrital quartz, dolomite and rare feldspar.
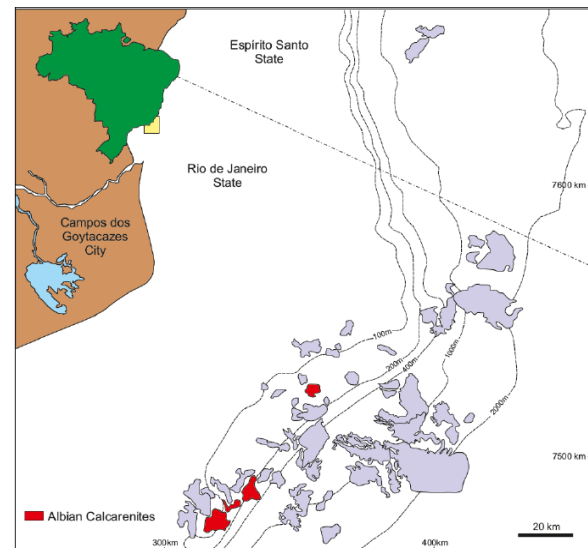

Figure 1 – Campos Basin's location map. In red, Albiancalcarenite reserves (modified from Bruhn et al., 2003)
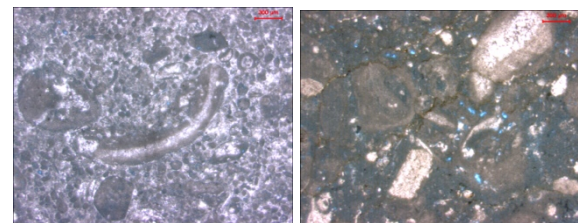

Figure 2 – Thin sections photomicrography of analyzed samples (red bar 300 μm): (Left) W2-01 (ϕ=16.3%, k=0.24mD) poorly sorted peloidal skeletal pack-grainstone; (Right) W2-03 (ϕ=21.9%, k=2.02mD) poorly sorted oncolitic peloidal skeletal packstone
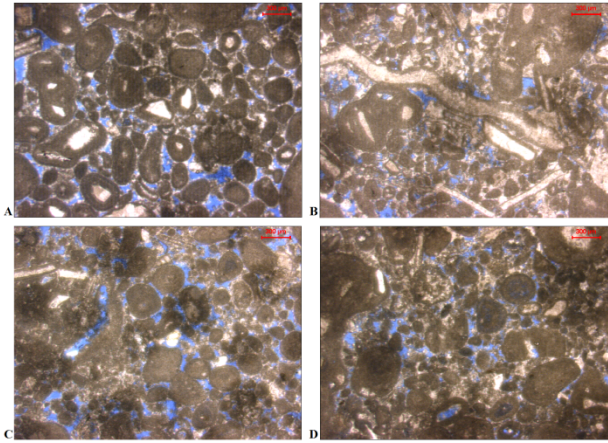
Figure 3 – Thin sections photomicrography of analyzed samples (red bar 300 μm): (A) W1-01 (ϕ=23.0%, k=8.95mD) moderately sorted oolitic grainstone within thin grain cement; (B) W1-02 (ϕ=25.7%, k=222mD) moderately sorted grainstone within calcite cement; (C) W1-05 (ϕ=28.9%, k=602mD) moderately well sorted peloidal skeletal grainstone within primary interparticle macropores and (D) W1-07 (ϕ=22.9%, k=9.78mD) poorly sorted oncolitic peloidal skeletal grainstone in which the primary interparticle pore network has been solution enhanced

Experimental Methods

Measurements of efective permeability were conducted on 1.5" plugs using a helium porosimeter, where the gas flow rate (q), outlet (P_0) and inlet (P_i) pressures were measured. After, the permeability was determined by Darcy's law for gasses – Eq. 1, where k is the permeability, μ is the fluid viscosity, L and A are, respectively, the length and the cross-sectional area of the sample, and P_{atm} is the atmospheric pressure.

$$q = \frac{kA}{2000\mu L} \frac{\left(P_0^2 - P_i^2\right)}{P_{atm}} \qquad (1)$$

X-ray diffraction and Rietveld method

X-ray diffraction (XRD) analysis and interpretation using the Rietveld method (Rietveld, 1969) was used to quantify the mineralogy of the rocks.

The quantitative analysis was made with the General Structure Analysis System (GSAS), software for Rietveld analysis and the difference between the measured and the adjusted curves was less than 3% for all cases.

X-ray Computed Microtomography

X-ray tomography is a non-destructive method that uses X-rays to produce tomographic images of a scanned sample, allowing the structures inside the sample to be studied without cutting it. Thereafter, reconstructions algorithms are used to generate a 3D image of the sample from the radiographic images.

Cubic samples with 2-mm long edges were prepared with a wire saw and scanned using two different systems: Xradia Micro XCT at University of Manchester and beamline I13 at Diamond Light Source (Oxford/UK).

For all the samples, the Xradia scanner was set up to work at 90 keV and 111μA, the magnification was 9.8X and pixel size of 1.1 μm. On I13, the x-ray energy was monochromated to 22 keV, and 1800 projections over a 180° rotation were captured with an exposure time of 6 seconds each. The pixel size was 1.125 μm. The samples did not exceed the field of view and the scan time for each sample was ~12 hour on the Xradia and ~4 hours on I13.

Avizo Fire 8.1 and an extension package (XSkeleton) were used for data filtering, segmentation and analysis.

Local and Global Parameters from X-ray CT

From a 3D image, it is possible to obtain global and local parameters. Global parameters are related to the whole pore space properties, such as micro- and macroporosity, specific surface area and tortuosity, whilst the local parameters are associated with properties of a single pore. These are mostly related to the specific properties of the pore, such as geometry, aspect ratio and roundness. The following parameters were collected:

Specific Surface Area (S): the ratio between the total pore surface area and total pore volume. In this study, S values range from 164mm^{-1} (for oolitic grainstones) to 721mm^{-1} (cemented grainstones).

Dominant Pore Size (DomSize): the upper boundary of pore radius of which 50% of the porosity on a 3D image is composed. This property is determined by the equivalent spherical diameter of each irregular pore. In this study, DomSize varies from 9.2μm (cemented grainstones) to 76.7μm (ooliticgrainstones).

Gamma (γ):defined for 2D images as the ratio between the perimeter and area (PoA) for a single pore normalized to a circle (Anselmetti et al., 1998). In this study, we reformulated this parameter for 3D images, defined as the specific surface area of a single pore normalized to a sphere (Eq. 2). It describes the sphericity of the pore and in our data gamma varies from 1.28 to 2.14. A γ value close to 1 (one) indicates that the pore is spherical, and as this number increases, the pore becomes flattened.

$$\gamma_{3D} = \frac{2}{3} \frac{\sqrt{A\pi}}{\sqrt[3]{\frac{16}{9}\pi^2 V}} \qquad (2)$$

Microporosity (ϕ_μ): the difference between gas porosity, measured on a core plug (ϕ_{gas}), and the macroporosity - ϕ_{CT}, obtained from the 3D image of the sample (Eq. 3).

$$\phi_\mu = \phi_{gas} - \phi_{CT} \qquad (3)$$

Tortuosity (τ): the ratio between the length of the path of the fluid inside the rock, and the straight distance between its end points. It was calculated by computing the centroid of each 2D image, and then the path length through the centroids and divides it by the number of planes multiplied by the resolution along the axis.

Coordination number: the number of pore throats connected to one pore. The average coordination number is defined as the ratio between the total number of pore throats and the number of pores in the sample. In this work, we created and analyzed the centerline tree (Figure

4A), where each segment represents a pore and nodes represent either the pore throats (junctions) or the pore edge. As the software does not differentiate pore throats and edges, the highest possible value is 2, which is the isolated pore case (two nodes and one segment). Increasing the number of connections, coordination number decreases, (Figure 4).

Although this methodology does not provide values of coordination number commonly reported in literature, which varies from 6 up to ~40 (Raoof and Hassanizadeh, 2010; Jivkov et al., 2013), it does differentiate the connectivity of the pore space. For our samples, coordination number varies from 1.36 to 1.99.
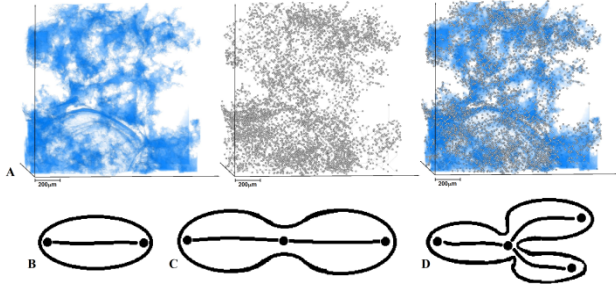

Figure 4 – (A) The skeleton of pore space (B) is the isolated pore case, (C) represents two connected pores, with coordination number of 3/2 and (D) shows three connected pore and coordination number of 4/3

Prior to the pore space analysis, the image was segmented into pores and matrix, where the pores are represented by the blue color and the matrix by the black color (Figure 5A). All the global parameters were extracted from this image, whilst local parameters were obtained from images such as Figure 5B, where the total pore space was separated into individual pores, and each color represents a different pore. Figure 5C shows a 3D rendering of this pore space.
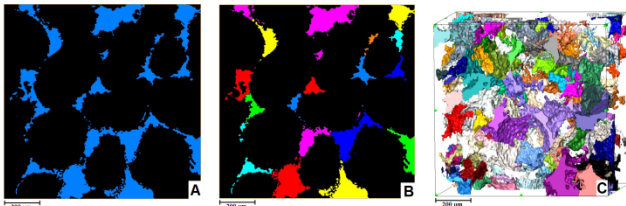

Figure 5 – (A) Binary image representing the pore space (blue) and the matrix (black); (B) The separated pore space; (C) Tridimensional representation of (B)

Kozeny's equation – Determination of permeability

The Kozeny equation (Eq. 4) is one of the most popular and fundamental correlations between permeability and porosity (Kozeny, 1927). It was derived from a rock model where the pore space is described as n capillary tubes, with the space between these tubes filled with a non-porous material. Later, Mortensen et al. (1998), redefined this equation and introduced the Kozeny´s factor (c) and expressed the permeability (k) in terms of this parameter, porosity (ϕ) and specific surface area (S) - Eq. 5. The Kozeny factor (c) varies from 0.15 to 0.25 as the porosity increases from 5 to 50%.

$$k = \frac{c\phi^3}{S^2} \quad (4)$$

$$c = \left(4\cos\left(\frac{1}{3}\arccos\left(\phi\frac{64}{\pi^3} - 1 \right) + \frac{4}{3}\pi \right) + 4 \right)^{-1} \quad (5)$$

Despite the reasonable adjusted coefficient (R^2 = 0.668) obtained between k_K (Kozeny's permeability) x $k_{measured}$. Figure 6, the model has a tendency to overestimate low (<100mD) and underestimate high (>100mD) permeabilities.

Statistical Model and Multiple Linear Regressions (MLR)

To improve the coefficient of determination, permeability (k_K) was combined with global and local geometrical parameters of the pore space by using MLR. Equation 6 describes the proposed model, where P_m is the measured property, P_e represents the estimated property, X_n represents global and local parameters β_n are coefficients determined by the regression, (Eq.6).

$$P_m = \beta + \beta_0 P_e + \beta_1 X_1 + \beta_2 X_2 + ... \quad (6)$$

This study focused upon determination of how this statistical model fits to the experimental data, analyzing the adjusted coefficient of determination $\left(\overline{R}^2 \right)$ estimated by Eq. 7, where n is the sample size and p is the total number of variables in the linear model. Unlike the R^2, $\overline{R}^2$ increases when a new independent variable is included only if it improves R^2 more than expected by chance, as it considers the degree of freedom of the dataset.

$$\overline{R}^2 = 1 - \left(1 - R^2\right)\frac{n-1}{n-p-1} \quad (7)$$

In a MLR, sample size must be large enough to ensure stable model coefficients. If not, the model may not generalize well beyond the current sample (Brooks and Barcikowski, 2012). To provide minimal shrinkage of the coefficient of determination, the ratio between sample size and predictors ranges widely: 10 to 1 (Miller and Kunce, 1973) to 30 to 1 as stated by Pedhazur and Schmelkin (1991). This work was developed with just eleven samples. Then, all the results obtained here reflect just the behavior of this set of data. Brooks and Barcikowski (2012) reported that a study with insufficient sample size stands a large chance of committing type I error (incorrect rejection of a true null hypothesis - "false positive") and II error (failure to reject a false null hypothesis - a "false negative"). For this reason, in addition to adjusted R^2 determination, p-value and statistical power were also calculated for each MLR. A small p-value (<0.05) and a high statistical power (>0.8) indicate that there is a low probability that these errors were committed in the MLR.

Results

Petrographical and 3D image analysis (Table 2a and 2b) reveal that the lowest porosity sample, W2-01 (Figure 2; 16.3%), has the lowest permeability (0.24mD).

Correspondingly, it has the lowest volume of macroporosity (1.44%), smallest dominant pore size (12.2μm) and highest specific surface area (721mm^{-1}), and largest coordination number (1.99). Conversely, the sample with the highest porosity (28.89%), W1-05 (Figure 3), has the highest permeability (602mD). Interestingly, it does not have the highest volume of macroporosity (10.61%, compared to a maximum of 11.50% in sample W1-02 (Figure 3)), largest dominant pore size (64.92μm, compared to a maximum of 76.7μm in sample W1-02), or lowest specific surface area (176mm^{-1} compared to a minimum of 163 mm^{-1} in sample W1-02). Sample W2-03 (Figure 2) is the sample with the highest volume of micrite in the dataset. Consequently, it has undergone more compaction than other samples. It has the highest (γ) of all the samples (2.14), but compared to other samples from this well, it has the highest volume of macroporosity (3.01%), largest DomSize (19.31μm) lowest S (516mm^{-1}). In contrast, sample W1-02 (Figure 3) has an excellent permeability (222mD) and the highest volume of macroporosity (11.5%) largest DomSize (76.7μm), and lowest S (163 mm^{-1}) of the dataset.

Qualitatively, therefore there appears to be a broad relationship between permeability and porosity. In general, as permeability increases, macroporosity, γ, and DomSize also increase, whilst S, AR, microporosity, coordination number and τ decrease (see Figures 7 to 12; Tables 2a and 2b). Nevertheless, the dataset reveals anomalies, which are apparently related to complexities in the pore geometry induced by compactation. This sample, W1-02, has the lowest volume of microporosity (55.2% of the total pore volume) of all samples. In comparison, the most micritic, least well sorted sample (W2-03), Figure 2, is highly compacted and is not the most microporous sample in the dataset (84.7% of total porosity is microporosity, compared with 96.9% in sample W2-02), nor has it the highest S or smallest DomSize, it is difficult to constrain the key control on permeability.

To improve permeability estimation, a MLR was used to examine the link between permeability, porosity and 3D DIA parameters obtained from X-ray tomography. The following steps incorporated a single 3D DIA parameter at a time as a linear combination to the estimated property. All arrangements were tested, but just the higher values of adjusted R^2 are shown in Table 1, where the p-value and statistical power are also presented.

Six predictors were used to estimate permeability: gamma (γ), DomSize, tortuosity (τ). Specific surface area (S), total porosity and its micro and macro fractions are implicit in this adjustment. A very strong correlation is observed in this MLR, the adjusted R^2 increases from 0.668 to 0.916 just by adding the dominant pore size (DomSize) to the model, as shown in Figure 13. By adding (γ), (φ$_μ$), (AR), (τ) and (φ$_{CT}$), a slightly improvement on $\overline{R}^2$ to 0.948 is observed. For all cases, p-value is always below 0.05 and the statistical power, for most of the cases, is greater than 0.8. This parameter is strongly related to the adjusted R2, showing values not desirable for $\overline{R}^2$ < 0.88.

Conclusions

This study successfully presents the quantification of local and global pore space parameters of carbonate rocks from 3D images obtained by X-ray tomography and how to incorporate them to a statistical model. Also, their influence on permeability was evaluated and the controlling parameters were determined. Our results show: (a) there is not a single parameter that controls the measured properties; multiple controls must be operating and these cannot be fully determined by geological observation alone; (b) effective porosity and DomSize are the major controlling factors of permeability, consistent with the fact that the flow mainly follows large pores during fluid transport. (c) the permeability estimated from Kozeny's equations combined with DomSize describes more than 91% of the measured permeability, an impressive adjustment as permeability prediction is still one of the greatest challenges in petrophysical analysis.

References

Ahr, W., 2008, Geology of Carbonate Reservoirs: The Identification, Description, and Characterization of Hydrocarbon Reservoirs in Carbonate Rocks, 1st ed.: Nova York. John Wiley& Sons Inc, 296 p.

Anselmetti, F. S., S. Luthi, G.P. Eberli, 1998, Quantitative characterization of carbonate pore systems by digital image analysis: AAPG Bulletin, v. 82, p. 1815 – 1836.

Brooks, G. P., R. S. Barcikowski, 2012, The PEAR Method for Sample Sizes in Multiple Linear Regression: Multiple Linear Regression Viewpoints, v. 38, p. 1 – 16.

Bruhn, C. H., J. A. Gomes, C. D. Lucchese Jr., P.R. Johann, 2003, Campos basin: reservoir characterization and management – historical overview and future challenges: Offshore Technology Conference, OTC 15220, Houston, Texas, p. 1 – 14. doi: 10.4043/15220-MS.

Castro, D. D., P. L. F. Rocha, 2013, Quantitative parameters of pore types in carbonate rocks: Brazilian Journal of Geophysics (RBGf), v. 31, p. 125-136.

Hollis, C., V. Vahrenkamp, S. Tull, A. Mukherji, C. Taberner, Y. Huang, 2010. Pore system characterization in heterogeneous carbonates: analternative approach to widely used rock-typing methodologies: Marine Petrololeum Geology, v. 27, p. 772 – 793.

Jivkov, A. P., C. Hollis, F. Etiese, S. A. McDonald, P. J. Withers, 2013, A novel architecture for pore network modeling with applications to permeability of porous media: Journal of Hydrology v. 486, p. 246 – 258. doi: 10.1016/j.jhydrol.2013.01.045.

Knofczynski, G. T., D. Mundfrom, 2008, Sample Sizes When Using Multiple Linear Regression for

Prediction: Education and Psychological Measurement, v. 68, p. 431 – 442.

Kozeny, J., 1927, Uber kapillare leitung des wassers im boden (Aufstieg versikerung und anwendung auf die bemasserung): Sitzungsber Akad, Wiss, Wein, Math- Nuturwiss, KL, v. 136, p. 271–306.

Miller, D. E., T. J. Kunce, J. T., 1973, Prediction and statistical ovekill revisited: Measurementand Evaluation in Guidance, v. 6, p. 157-163.

Mortensen, J., F. Engdtrom, I. Lind, 1998, The relation among porosity, permeability, and specific surface of chalk from the Gormfield, Danish North Sea: SPE Reservoir Evaluation & Engineering, v.1 p. 245 – 251.

Pedhazur, E. J., L. P. Schmelkin, 1991, Measurement, design, and analysis: An integrated approach: New Jersey, Psychology Press, 840 p.

Raoof, A., S. M. Hassanizadeh, 2012, A new formulation for pore-network modeling of two phase flow: Water Resources Research, v. 48, p. 1 – 13. doi:10.1029/2010WR010180.

Rietveld, H. M., 1969, A profile refinement method for nuclear and magnetic structures: Journal of Applied Crystallography, v. 2, p. 65 – 71.

Weger, R. J., G. P. Eberli, G. T. Baechle, J. L. Massaferro, Y. Sun, 2009, Quantification of pore structure and its effect on sonic velocity and permeability in carbonates: AAPG Bulletin, v. 93, p. 1297 – 1317. doi:10.1306/05270909001.

Table 1 - Adjustes coefficient of determination between measurement and stimated permeability

Parameters used to predict permeability	Adjusted R^2	p-value	Statistical Power
k_K	0.668	0.0013	0.66
k_K + DomSize	0.916	0.0001	0.98
k_K + DomSize + γ + ϕ_μ + AR + τ + ϕ_{CT}	0.948	0.010	0.99

Table 2a - Local and global parameters obtained from 3D images

Samples	Macro ϕ (%)	Aspect Ratio (AR)	S (mm^{-1})	γ	τ
W1-01	8.26	0.546	188	1.77	2.88
W1-02	11.52	0.544	163	1.79	2.59
W1-03	2.59	0.575	218	1.54	7.89
W1-04	4.55	0.575	189	1.65	3.47
W1-05	10.61	0.574	176	1.71	2.97
W1-06	6.49	0.575	254	1.67	2.94
W1-07	4.21	0.577	235	1.58	4.02

Table 2b - Local and global parameters obtained from 3D images

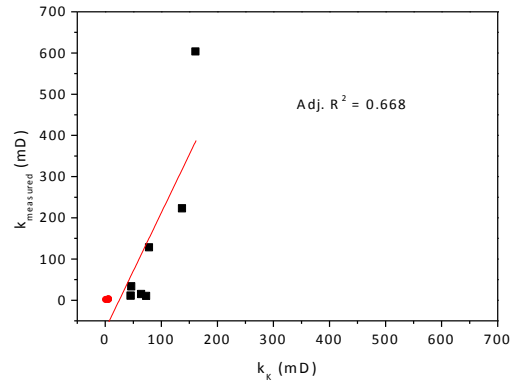| Samples	DomSize (µm)	Coord. number	Microϕ (%)	Micropores %
W1-01	73.69	1.85	14.77	64.13
W1-02	76.70	1.80	14.19	55.19
W1-03	41.11	1.93	19.48	88.26
W1-04	53.22	1.57	17.72	79.57
W1-05	64.92	1.39	17.90	62.78
W1-06	46.66	1.67	22.40	77.57
W1-07	41.89	1.36	18.67	81.60

Figure 6 – k_K x $k_{measured}$. Cemented grainstone are represented by circles and oolitic grainstone by squares
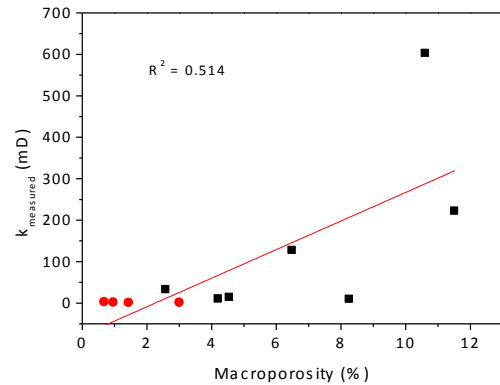

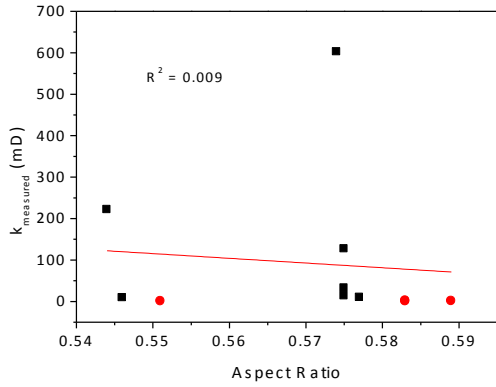Figure 7 – Cross-plot shows a trend with increase in values of $K_{measured}$ and macroporosity

Figure 8 – Cross-plot shows a trend with a slightly decrease in values of $K_{measured}$ and aspect ratio (AR)
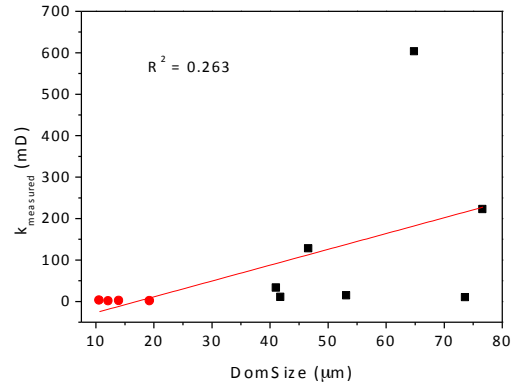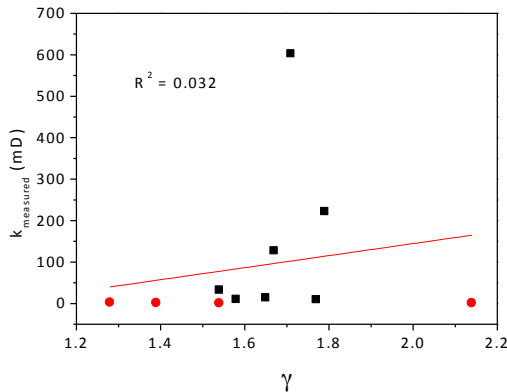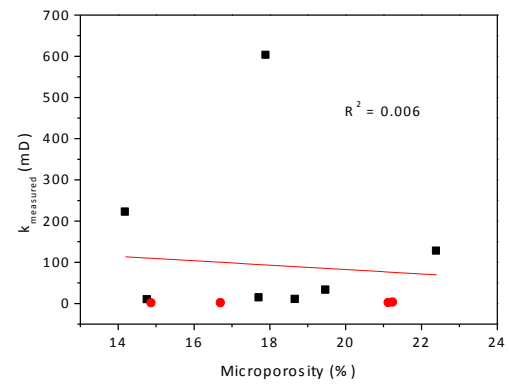

Figure 9 – Cross-plot shows a trend with a slightly increase in values of $K_{measured}$ and gamma (γ)

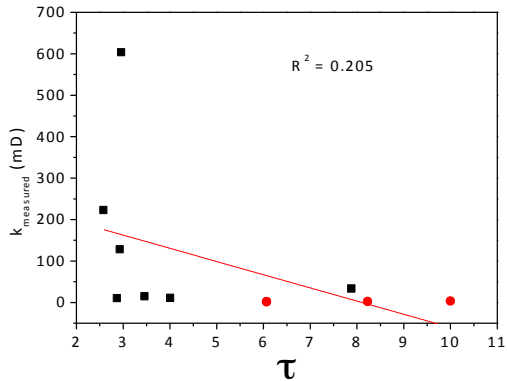Figure 10 - Cross-plot shows a trend with a decrease in values of $K_{measured}$ and tortuosity (τ)

Figure 11 - Cross-plot shows a trend with an increase in values of $K_{measured}$ verus DomSize

Figure 12 – Cross-plot shows a trend with a slightly decrease in values of $K_{measured}$ and microporosity
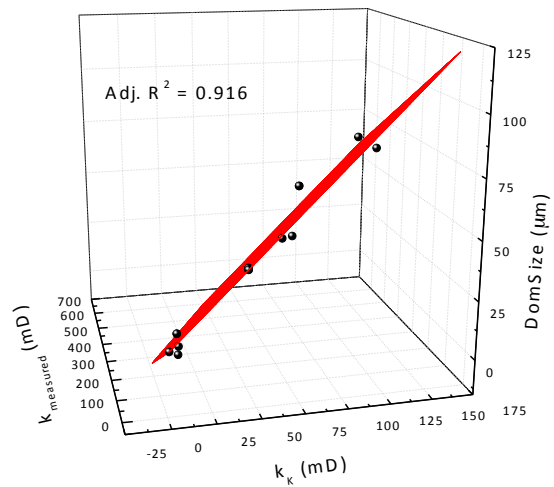

Figure 13 – 3D crossplot of the relationship between DomSize, $k_{measured}$, k_K. Observe the importance of the dominant pore size as factor controlling permeability